Materials Science & Engineering A 841 (2022) 143036

Contents lists available at ScienceDirect

Materials Science & Engineering A

journal homepage: www.elsevier.com/locate/msea

Deformation and cracking phenomena in cold sprayed 6061 Al alloy powders with nanoscale aluminum oxide films

A. Navabi [a], M. Vandadi [a], T. Bond [b], V. Rahneshin [a,b], J. Obayemi [b], R. Ahmed [b], J.E. Oghenevweta [b], V. Champagne [c], N. Rahbar [a,b,*], W.O. Soboyejo [b,**]

[a] Department of Civil and Environmental Engineering, Worcester Polytechnic Institute, Worcester, MA, 01609, USA
[b] Materials Program, Department of Mechanical Engineering, Worcester Polytechnic Institute, Worcester, MA, 01609, USA
[c] Army Research Laboratory, Aberdeen Proving Ground, MD, 21005, USA

ARTICLE INFO

Keywords:
Cold spray
Atomistic simulations
Cracking
Oxide layers
Bonding
Deformation mechanisms

ABSTRACT

This paper presents deformation and cracking phenomena associated with the cold spray of nanoscale surface oxide layers associated with the cold spray of 6061 Al alloy powders. The structure of the top surface oxide film was revealed via Focused Ion Beam (FIB), Transmission Electron Microscopy (TEM), and X-ray Photoelectron Spectroscopy (XPS). The observations show the oxide layer characteristics most likely matches crystalline γ-Al_2O_3. Phenomena associated with surface contacts, contact-induced elastic-plastic deformation, heating, and cracking are then studied using a combination of analytical models, Finite Element Analysis (FEA) and Molecular Dynamics (MD) simulations. MD simulations are also used to obtain estimates of oxide film young's moduli, strains to failure, and the fracture energies of oxide films. The results from the MD simulations and microscopy observations are incorporated into a bi-linear Johnson- Cook finite element simulations of cold spray contact-induced deformation and cracking due to the impact of aluminum powder particles with nanoscale oxide layers and similar substrates with nanoscale oxide layers. The powder impacts are shown to result in localized splat deformation and heating, along with the cracking of the oxide layers that expose fresh metallic surfaces to high temperature surface contacts (at temperatures above the recrystallization temperature for aluminum/6061 Al) that can give rise to bonding and mechanical interlocking. The implications of the results are then discussed for the design of cold spray processes for the fabrication and repair of 6061 Al structures.

1. Introduction

Cold spray (CS) is an additive manufacturing technology that allows for the dense deposition of materials at temperatures that are well below their melting points [1–5]. The process involves the acceleration of micron-sized particles to high velocities (usually between 200/300 m/s and 1200 m/s) to adhere to various substrates upon impact [1–2], [6–7]. For powder contacts above a critical velocity, the particles bind to the substrate by processes that have been attributed to the role of adiabatic shear, plasticity, intermixing, and mechanical interlocking [8–13].

However, the insights provided by recent studies [14–19] suggest that the cold spray of Al/6061Al powders is also influenced by nanoscale oxide and hydroxide layers. These layers are formed on the surfaces of the powders and the substrates during exposure to the ambient environment or the packaging environment that is used for the storage of the powders. Rahmati et al. used numerical and experimental methods to show that the oxide layer drastically influences the bonding mechanism and that having thicker oxide layers would result in inferior adhesion between the powder and the substrate [20]. Additionally, Hameda et al. used smoothed particle hydrodynamics method to simulate the cold spray impact, which showed that the presents of oxide particles along with voids at the powder/substrate intersection lowers the quality and efficiency of the bonding in the cold spray process [21]. The studies have also revealed that a nanoscale oxide layer with a thickness of about 5-nm (after exposure to a relative humidity below 95%) exists on the surface of the 6061 Al alloy particles. In most cases, however, hydroxide layers have only been reported on the surfaces of Al/6061Al powders exposed to environments with relative humidity above 95% [14].

There is, therefore, a need to consider the role that surface oxides play in the cold spray processing of 6061 Al powders since most of the

* Corresponding author. Department of Civil and Environmental Engineering, Worcester Polytechnic Institute, Worcester, MA 01609, USA.
** Corresponding author.
E-mail addresses: nrahbar@wpi.edu (N. Rahbar), wsoboyejo@wpi.edu (W.O. Soboyejo).

https://doi.org/10.1016/j.msea.2022.143036
Received 25 January 2022; Received in revised form 23 March 2022; Accepted 24 March 2022
Available online 31 March 2022

cold sprayed powders are stored in environments with relative humidity below 95% [22]. Hence, in this paper, we present the results of a combined experimental and computational study on the effects of nanoscale oxide layers on the contacts between 6061 Al powders and 6061 Al alloy substrates with nanoscale oxide layers that are relevant to cold spray in environments with relative humidity below 95%. Molecular dynamics simulations are used to study the nanoscale deformation and cracking of aluminum oxide layers on 6061 aluminum powders. The MD simulations are utilized to compute basic materials properties (Young's moduli, strength, fracture energies) that are incorporated into finite element simulations of the impact of aluminum oxide layers on 6061 Al powders that are cold sprayed onto aluminum oxide layers on 6061 Al substrates.

This paper is divided into 5 sections. Following the introduction (Section 1), powder size distributions and powder oxide layers are characterized using a combination of microscopy techniques in Section 2. The combined MD and finite element methodology and parameters are then presented in Section 3. This is followed by Section 4 in which the results obtained from the simulations are discussed, before presenting the salient conclusions arising from this study in Section 5.

2. Materials and method

2.1. Materials and powder characterization

The gas atomized cold spray 6061 aluminum alloy powders used in this study were obtained from VRC Inc. in Webster, MA. The microstructure of the powder particles was characterized using JEOL JSM-7000F Schottky field emission gun-scanning electron microscopy (FEG-SEM) equipped with an 80 mm^2 X-Max^N energy dispersive X-ray spectroscopy (EDS) silicon drift detector, and the results are shown in Fig. 1(a). It can be observed from the SEM images (Fig. 1a) that the gas atomization process resulted in nearly spherical particles which consist of elongated grains that are formed during the solidification process.

Powder size ranges were characterized using the ImageJ software package (Image J, NIH, Bethesda, MD). The ImageJ analysis utilized the SEM images of the powder in a contrast thresholding technique that was used to determine the area of the particles in the image, as shown in Fig. 1(b and c). Fig. 1 (b) & (c) shows the powder size distributions and the grain size distributions, respectively. In Fig. 1(b), the powder sizes were generally in a range between 6 and 60 μm, with an average particle size of about 29 μm. This is within the range that has been reported previously for 6061 Al by other researchers [23–25]. As shown in Fig. 1 (c), the revealed average grain sizes were found to be about 3 μm. The range of grain sizes is also between 1 and 5 μm.

The surface chemical histories and the bonding states of the surface components were then assessed using XPS. The XPS characterization of the powders was carried out using a PHI5600 XPS system with a third-party data acquisition system (RBD Instruments, Bend Oregon). The analysis chamber base pressure was kept at $<1 \times 10^{-9}$ Torr. Photoelectrons were collected using hemispherical energy analyzer that was positioned at 90° with respect to the incoming monochromated Al Kα X-ray flux and 45° with respect to standard sample positioning. The survey spectra were acquired using a 117 eV pass energy, a 0.5 eV step size, and a 50-ms-per-step dwell time while the high-resolution spectra were obtained using a 23.5 eV pass energy, 0.025 eV step size, and a 50 ms dwell time per step. Post-acquisition data analysis was carried out using the commercial CasaXPS2.3.15 software.

Fig. 2 shows the XPS results obtained for the 6061 Al powder particles with diameters of 29.4 ± 10 μm. The XPS results confirm the presence of Al, Mg, and Si, which are the primary elements in the 6061 Al alloy, as well as O, which is attributed to the presence of oxide film, as shown in Fig. 2(a). It should be noted that the carbon peaks in Fig. 2(a) are attributed to the presence of impurities. Fig. 2(b–d) show the core-level high-resolution scan spectra for Al *2p*, O *1s*, and Mg *1s*, acquired to understand the chemical histories of the top surface of the specimen.

The deconvolution of the Al *2p* XPS spectrum revealed three distinct broad peaks that were fitted with three Gaussian-Lorentzian curves (Fig. 2(b)). The binding energies for these peaks are located at 76.81 ± 0.01, 74.11 ± 0.02, and 71.41 ± 0.01 eV, corresponding to bonding characteristics assigned to Al octahedrally coordinated with O (oxide-film), Al at the metal/oxide interface (surface-oxide), and metallic Al, respectively [26–30]. The binding energy of 76.81 ± 0.01 eV is typically assigned to energies that are associated to Al_2O_3, especially, crystalline

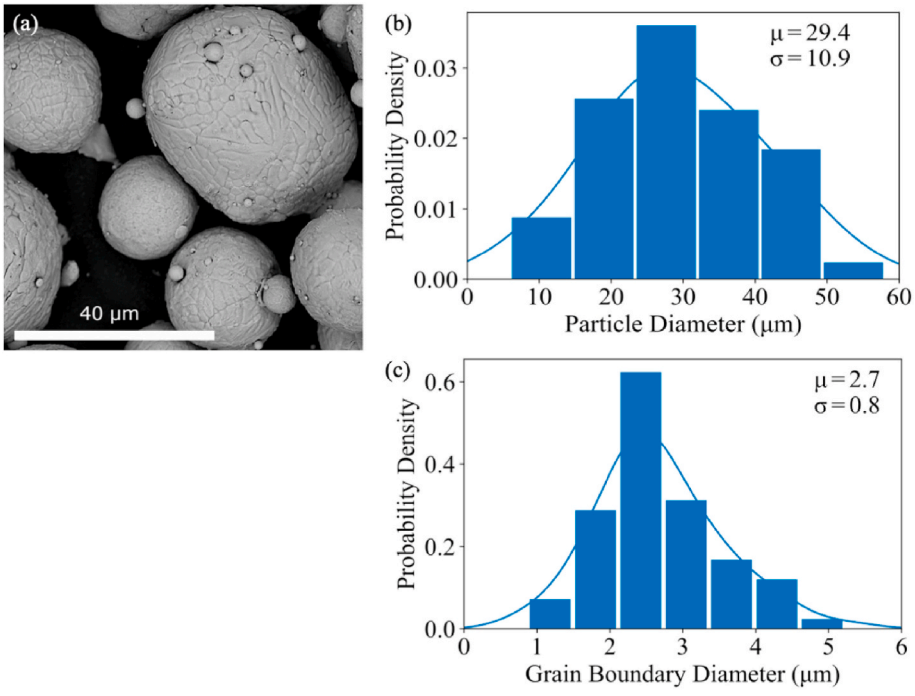

Fig. 1. (a) SEM microstructure of the gas atomized 6061 aluminum alloy powder showing size and shape of powder particles as well as cellular structures on the surface of the powders; (b) Particle size distribution analysis; (c) Histogram showing the grain diameters within the powder.

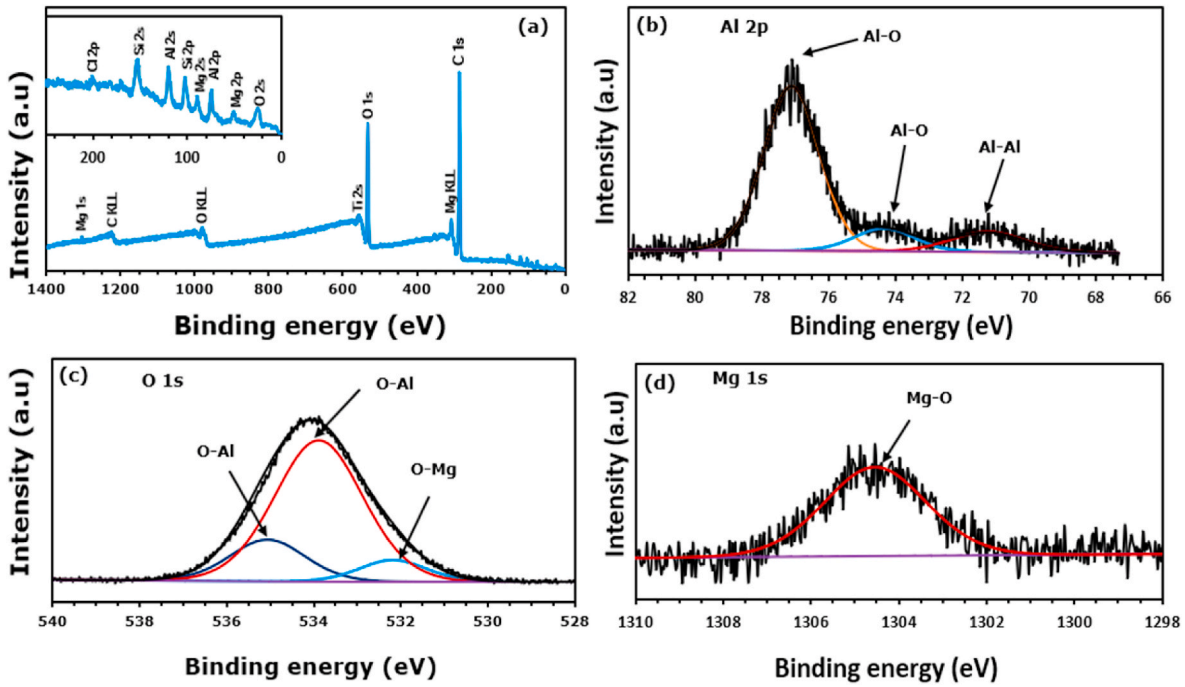

Fig. 2. XPS spectra obtained for the 6061 Al powder particles within 1–10 nm of the powder surface showing, (a) XPS survey scan spectrum with weaker XPS peaks (insert), and (b–d) High-resolution spectra obtained for the Al 2p, O 1s, and Mg 1s peaks, respectively. The survey scans and the high-resolution spectral regions were calibrated such that the primary adventitious C 1s peak is centered at 284.8 eV. The surface composition consists of high amounts of carbon and oxygen shown in the fine XPS survey as well as contributions from the Al 2p, O 1s, and Mg 1s components.

γ-Al_2O_3, as reported in Refs. [26–28]. In comparison with [28–30], where slight lower binding energies were reported for aluminum oxides, the Al–O curves (Fig. 2(a)) slightly shifted to higher binding energies with respect to the binding energy of metallic Al located at 71.41 ± 0.01 eV. Such high binding energy shift has been previously attributed to the thickness of the oxide film formed on the Al substrate, induced most likely by defect states within the band gap in the Fermi level of the oxides [26]. The 76.81 ± 0.01 eV oxide film (γ-Al_2O_3) was found to constitute approximately 86.53% of the component phases in the Al *2p* spectrum.

In the O *1s* deconvolution (Fig. 2(c)), the identification of the oxygen signal was observed to consist of binding energy components, centered at 535.01 ± 0.2 eV and 533.88 ± 0.1 eV, attributable to the Al oxide-film and oxide-surface layers [26], and a component at 531.82 ± 0.1 eV, attributable to oxygen bonded to magnesium [28–30]. The Al–O component phases were estimated to constitute to approximately 93.36%, with Mg–O component consisting of lean percentage. When the Mg *1s* was deconvoluted, a single Gaussian-Lorentzian curve was determined, with its peak and binding energy being located at 1304.53 ± 0.1, as shown in Fig. 2(d). This peak is attributed to Mg bonded to O [29,30]. The oxidation characteristics at the top surface layer using XPS has indicated a high percentage concentration of Al oxides, most likely crystalline γ-Al_2O_3, with some incidence of magnesium oxide occurring with a very lean concentration.

The detailed microstructures of the Al 6061 powder particle and the oxide layers were examined using S/TEM, HRTEM, and STEM-EDS mapping. Data were acquired using a JEOL ARM-200F high resolution TEM (110pm) and high angle annular dark-field (HAADF) STEM (78pm), and energy resolution (0.33eV) analytical instrument equipped with Cold Field Emission Gun source, Gatan UltraScan 1000XP CCD camera (4k x 4k) and a JEOL Centurio SDD EDS detector with 100 mm^2 detection area and also fitted with advanced Cs spherical aberration-corrector for the condenser lens and a GIF Quantum image filter electron energy loss spectrometer (EELS), operated at 200 kV. The HAADF imaging was carried out with an inner collection semi-angle of ~80 mrad and an outer collection semi-angle of 160 mrad. The lattice spacings were processed by using the Gatan DigitalMicrograph software equipped with HRTEM tools.

Figs. 3 and 4 show the BF-STEM, STEM-EDAX, and HRTEM imaging of FIB-cut cross-sections of the powder particles. A thin slice of a gas-atomized 6061 aluminum alloy powder particle was obtained by FEI Helios 660 focus ion beam scanning electron microscope (FIB-SEM) to produce a TEM specimen of about 100 nm. Using the Omniprobe® mechanical probe, the specimen was lifted and assembled on Cu lift-out grid for final thinning, polishing, and cleaning. Fig. 3(a and b) shows the Pt and C deposition layers as well as the presence of possible inclusion in the Al substrate. Fig. 3(b) shows a higher magnification BF-STEM image of SEM-FIB cut cross-section of the powder particle. It revealed the two layers of deposition comprising a carbon layer with ~50 nm (brighter color), and a platinum coating layer with ~650 nm (darker color) that protect the virgin oxide layer from gallium ions during milling. Fig. 3(c) shows a high magnification STEM image obtained to assess the detailed microstructure of the inclusion found in the Al powder particle (Fig. 3 (a)). STEM-EDAX analysis (results not included) shows that the inclusion is made of three distinct intermetallics (β-Al5FeSi, π-Al8FeMg3Si6, and θ-Al2Cu), most likely formed during the gas atomized processing of the 6061 Al powder particles.

Fig. 4 shows the HAADF, EDAX, and HRTEM results obtained to better understand the chemistry of the oxide layer on a FIB-cut cross-sectional specimen that was analyzed within 5 min of extraction. The oxide thickness content was assessed by obtaining line scans from the cross-sections at locations where the metal/oxide and oxide/Pt-cap interfaces are edge-on, as shown in Fig. 4 (a & b) while HRTEM was employed to assess the detailed microstructure of the oxide layer at higher magnification (Fig. 3(c)). The oxide film thickness was then measured from the trace of the oxygen signal by taking the full width at half maximum (FWHM) to take account beam broadening within the sample and was found to be approximately 5.2 nm, a value of surface oxide thickness that lies within range of values that has been previously reported in the literature [28–30].

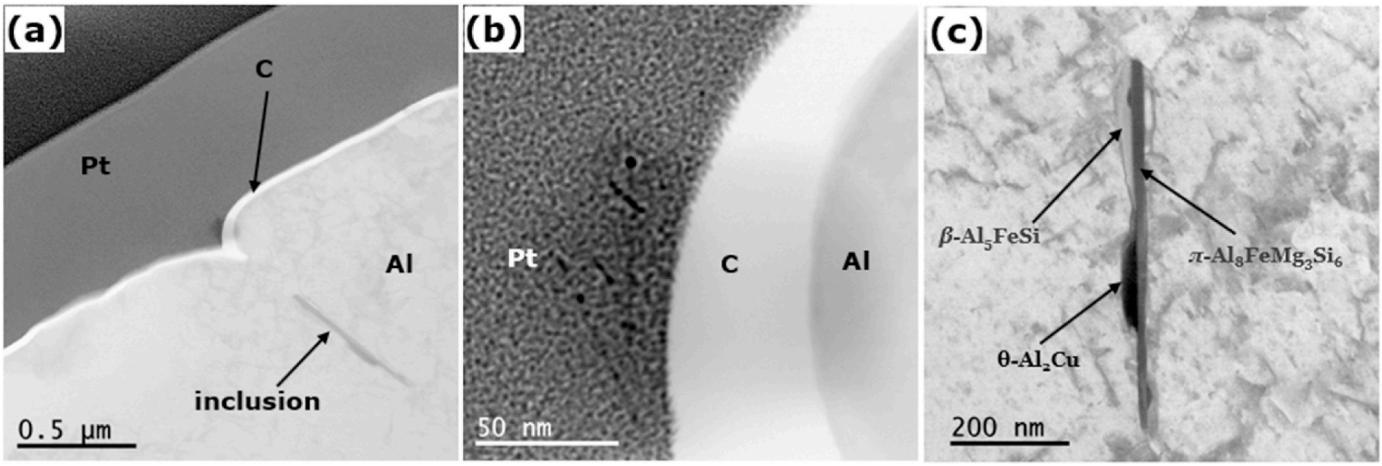

Fig. 3. BF-STEM microstructures from a FIB-cut cross section through the surface of 6061 Al powder particle showing: a) Low magnification revealing regions of deposition layers and 6061 Al powder particle, (b) Higher magnification of BF-STEM image revealing distinct Pt and C layers of deposition and Al powder particle, and (c) Higher magnification of BF-STEM image revealing formation of intermetallics.

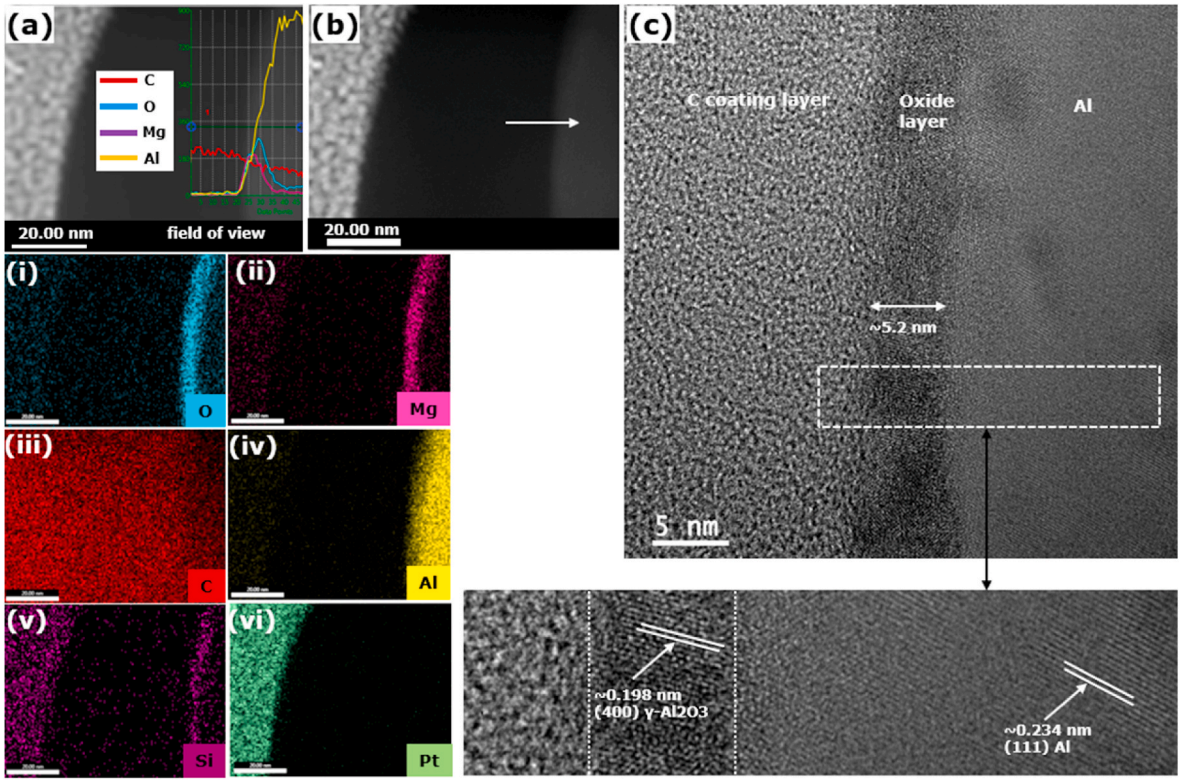

Fig. 4. STEM-EDAX data collected from a FIB-cut cross section through the surface of 6061 Al powder particle: a) line scan data acquired from the position as indicated by the white arrow in the STEM-HAADF image in (b). (i-vi) are high resolution X-ray maps extracted from (a); and (c) HR-STEM image obtained from the region as indicated by white box insert in the STEM-HAADF image in (b) showing distinct outer oxide layer on the 6061 Al powder particle.

We observed that there was consistent increase in the Mg, O, and Al signals within the oxide layer in the line scans (Fig. 4(a)) that were obtained from the region marked with the white arrow in Fig. 4(b). The white arrow is used to show the direction in which the line scans were acquired. Additional evidence of the consistent increase in Mg, O, and Al signals are clearly observed in the normalized X-ray maps corresponding to the background-subtracted EDAX signals from O, Al, Mg, Si and Pt, respectively (Fig. 4a(i-iv)).

The position of the oxide layer is clear from the O map (Fig. 4(a)i), and clearly, there is an enhancement in the Mg signal at the outer oxide layer of the O signal (Fig. 4(a)ii). When these high-resolution maps were overlayed (result not shown), the Mg was observed to concentrate towards the top surface of the oxide layer with thickness of about 2 nm. The observation of Mg-rich signal at the outer layers of gas-atomized 6061 Al has been previously reported [23,28], where the formation of preferential amorphous or crystalline Mg-rich oxides depending on heat treatment has been reported by similar analytical techniques.

Additionally, in the HRTEM image (Fig. 4(c)), detailed microstructure of the oxide layer at a very high magnification revealed evidence of crystal/lattice fringes, suggesting possible presence of crystalline phase (s) in the oxide layers. When these crystal fringes were measured with an error of 0.02% nm, d-spacings of 0.239 nm and 0.198 nm were

predominantly found to exist in the oxide layer. These d-spacings were found to match the (311) and (400) reflections of γ-Al_2O_3, respectively. It should be mentioned that $MgAl_2O_4$-spinel have been reported to have almost identical structural information with γ-Al_2O_3 as seen in the d-spacings of $MgAl_2O_4$-spinel with 0.244 nm and 0.202 nm corresponding to its $d_{(311)}$ and $d_{(400)}$ reflections [60,61]. Such similarities have been attributed to γ-Al_2O_3 of being the defect-structure of $MgAl_2O_4$-spinel with both having cubic structure.

Typically, the formation of surface oxides in Al–Mg alloys have been widely investigated and various reports have shown that amorphous Mg-rich oxide top surface layers are possibly formed at lower temperatures while at relatively higher temperatures these amorphous phases could crystallize to form either combination or single phases of $MgAl_2O_4$, defect inverse $Al(Mg,Al)_2O_4$ or γ-Al_2O_3 at the oxide/metal interface, especially when there is selectively outward diffusion and oxidation of Mg at the free surface [28,30].

In the line scan, as shown in Fig. 4(a)ii, Mg is selectively segregated to the top outer surface. Such segregation may likely form Mg-rich oxidation top surface products that are most likely amorphous since there were no crystal fringes that match either the highly favored spinel $MgAl_2O_4$ or MgO oxides at the oxide layer, as shown in Fig. 4(c). Thus, when the XPS, STEM-EDAX, and HRTEM results are combined, we conclude that the 6061 Al powder has topical nanoscale crystalline oxides (approx. 5.2 nm thick) on a substrate of crystalline 6061Al. The presence of Mg oxide products is also revealed by XPS and STEM-EDAX, albeit with lean concentrations and possibly amorphous structure.

3. Multiscale modeling

The details of the finite element modeling, and molecular dynamics simulations are presented in this section. The simulations were informed by the structure of the oxide layers from the HRTEM images of aluminum alloy powders that were presented earlier. The MD simulations were used to compute basic mechanical properties that were then incorporated into finite element simulations of contact-induced deformation, cracking and heating phenomena.

3.1. Molecular dynamics simulations

To model a representative powder-substrate impact that includes the oxide layer, higher-scale simulations methods, such as finite element analysis, require realistic material properties of the nanoscale oxide layer.

Estimates for Young's modulus and the ultimate tensile strength were computed from MD simulations of a 5 nm thick γ-alumina nanocrystal with constant deformation rates corresponding to the particle incident velocities in cold spray. As seen in Fig. 4, the oxide film consists of an oxidized layer that includes γ-alumina in the form of nanocrystalline grains. To obtain the necessary mechanical properties for the nanocrystalline phase of the oxide film, a 5 nm nanocrystal structure of γ-alumina was simulated with coordinate inputs of 10,368 and 7776 total aluminum and oxygen atoms with 3.99 to 2.66 ratio, respectively. Unit-cell was obtained from *ab-initio* calculations for an FCC γ-alumina having the symmetry space group of fd $\overline{3}$ m, with cell parameters of a = b = c = 7.887 Å and α = β = γ = 90° [31].

Periodic boundary conditions were applied along [100] and [010] of the 5 nm thick structure. Periodicity along [001] on the Z axis is removed once the application of stress is initiated perpendicular to (0001). Therefore, periodic boundaries will only be parallel to the (0001) plane or a and b directions of the simulation box, representing a thin-film of γ-alumina. Energy minimization of the system is done by iteratively adjusting the atomic coordinates of the 3D structure for 2 ps. Following geometry optimization, Nose-Hoover thermostats and barostats were applied to perform canonical and isothermal-isobaric ensembles for 750 fs each, respectively resulting in, stabilized system energy and proper domain dimensions. All simulations were carried out using the COMB-3, third generation of Charge-Optimized Many-Body, potential function [32,33]. LAMMPS (Large Atomic/Molecular Massively Parallel Simulator) [34] was used for performing simulations. The charge equilibration (Qeq) method was used for charge prescription, with atomic masses of 16 amu and 26.98 amu for oxygen and aluminum, respectively.

Corresponding to the ranges reported in earlier work for the cold spray of aluminum particles [6,35,36], the velocity of the most outer layer, within the oxide-layers participating in impact, was chosen to be 800 m/s during simulation.

3.3. Finite element models

Much work has been done on the modeling of cold spray impacts of aluminum or aluminum alloys on corresponding substrates [37–44]. Here, we have created a FEA model that considers realistic oxide layers (with thickness of around 5-nm) along with the use of the Bilinear Johnson-Cook plasticity model for the aluminum. While there has been a plethora of research on the use of the Johnson-Cook (JC) plasticity model, due to ultra-high strain rate regime experienced during cold spray impact (~10^6), the use of a more complex constitutive model, capable of modeling a two-stage strain rate sensitivity is required [45].

The linear JC model (Equation (1)) is made bilinear by adding a second constant, C_2, to obtain an improved approximation of the strain rate sensitivity term in the constitutive model for the higher strain rate domain [45,46]. The resulting bilinear Johnson-Cook (BJC) equation is shown below in Equations (2) and (3).

$$\sigma = (A + B\varepsilon^n)\left[1 + Cln\left(1 + \frac{\dot{\varepsilon}}{\dot{\varepsilon}_0}\right)\right]\left(1 - \left[\frac{T - T_{transition}}{T_{melt} - T_{transition}}\right]^m\right) \tag{1}$$

$$C = \begin{cases} C_1 & \dot{\varepsilon}_p < \dot{\varepsilon}_c \\ C_2 & \dot{\varepsilon}_p \geq \dot{\varepsilon}_c \end{cases} \tag{2}$$

where $\varepsilon, \dot{\varepsilon}$, $\dot{\varepsilon}_0$, T, $T_{transition}$, T_{melt}, and $\overline{\sigma}$ are strain, strain rate, reference strain rate, absolute temperature, reference temperature, melting point of the material, and flow stress based on Johnson-Cook, respectively. A, B, n, C, and m are material constants. By substituting these terms with approximate terms, the following constitutive equation is derived:

$$\overline{\sigma} = \left[A + B\left(\overline{\varepsilon}^{pl}\right)^n\right]\left[1 + Cln\left(\frac{\dot{\overline{\varepsilon}}^{pl}}{\dot{\varepsilon}_0}\right)\right](1 - \widehat{\theta}^m). \tag{3}$$

The $\widehat{\theta}$ term in the equation above is the relative temperature, which is defined using the following equation:

$$\widehat{\theta} \equiv \begin{cases} 0 & \text{for } \theta < \theta_{transition} \\ (\theta - \theta_{transition})/(\theta_{melt} - \theta_{transition}) & \text{for } \theta_{transition} \leq \theta \leq \theta_{melt} \\ 1 & \text{for } \theta > \theta_{melt} \end{cases} \tag{4}$$

and $\overline{\varepsilon}^{pl}$ and $\dot{\overline{\varepsilon}}^{pl}$ are equivalent plastic strain and equivalent plastic strain rate.

To model failure in the model, we use dynamic failure, as described in the following equations:

$$\omega = \sum\left(\frac{\Delta\overline{\varepsilon}^{pl}}{\varepsilon_f^{pl}}\right) \tag{5}$$

$$\overline{\varepsilon}_f^{pl} = \left[d_1 + d_2\exp\left(d_3\frac{p}{q}\right)\right]\left[1 + d_4\ln\left(\frac{\dot{\overline{\varepsilon}}^{pl}}{\dot{\varepsilon}_0}\right)\right](1 + d_5\widehat{\theta}) \tag{6}$$

where d_1 to d_5 are failure parameters, measured at or below the transition temperature, p is the pressure stress, q is the Mises equivalent stress, and $\Delta\overline{\varepsilon}^{pl}$ is the incremental increase in the equivalent plastic strain. The Bilinear Johnson-Cook (BJC) is used here because JC un-

derestimates the flow stress for strain rates that are greater than 1000 s^{-1} for Al-6061 [44]. Previous work shows that experimental data on flow stress can be represented well by using a bilinear strain rate coefficient C. Therefore, a custom BJC plasticity VUMAT was developed to better account for both high and low strain rate regions during cold spray impacts within the ABAQUS modeling platform. Material parameters for 6061 Al in the BJC model were used from experimental work by other researchers. These are presented in Table 1.

The simulations of contact and heating were performed in ABAQUS-Explicit. For these simulations, a hard contact was assumed between the layers and the oxides were modeled as a shell layer that is tied to their corresponding aluminum to ensure they deform together. The substrate was fixed in location and the particle started with an initial velocity normal to the substrate. Hexagonal elements were used for the substrate, while tetragonal elements were used for the particles. For both hexagonal and tetragonal elements (substrate and particle meshes), a mesh sensitivity study was performed and an element size equal to $\frac{1}{30}d_p$ was used where d_p is the diameter of the particle. This element size was chosen after performing analysis on different sizes of the mesh. The simulations were performed under baseline conditions to figure out the correct element size. For the oxide layer, shell elements were used. The seed size used for these elements was set equal to $\frac{1}{50}d_p$ as well where d_p is the diameter of the particle.

Several parameters were varied over a range to study each parameter's effect on the behavior of the cold spray particle impact. While each parameter is studied, other parameters were kept constant at the baseline value. The velocities were changed from 600 m/s to 900 m/s with increments of 100. The baseline value for the velocity was 800 m/s. These velocities were selected to be from lower than the critical velocity of aluminum deposition up to higher than the critical velocity. The particle radius was changed from 5 μm to 25 μm with increments of 5 μm and a baseline value of 15 μm that was chosen from the range of particle sizes in Fig. 1. Finally, the oxide thicknesses of 2, 5, 8, 10 nm were simulated with 5 as the baseline value. As seen in the TEM images, the oxide thickness is around 5 nm.

Based on prior experimental results for the critical velocities of cold spray processing by Schuh and co-workers [10], the critical velocity for cold spray processing was estimated to be approximately 800 m/s [6,15,48]. The upper limit to the crack velocity was also estimated from the equation for the speed of sound in alumina, ($\sqrt{E/\rho}$) [48,49], where E is young's modulus of alumina and ρ is the density of alumina. Hence, the speed of sound in alumina was estimated to be about 9000 m/s. Therefore, for a 5-nm thick alumina layer, the time required for a dynamic crack to grow through the thickness of the oxide film is about 0.55 ps. On the other hand, a significant temperature rise occurs (due to cold spray powder impacts with the substrate) within nanosecond times scales, as shown in Fig. 5 where heat transfer in the system is simulated. As a result, the crack growth across the alumina layer occurs at a much faster rate than the rate of temperature increase. It is, therefore, reasonable to assume that brittle cracking is dominant mechanism in comparison to phonon transport and will occur in the alumina layer at temperatures that are close to room temperature (approx. 25C).

Brittle cracking damage criteria were used to model the cracking of the oxide layer on the particles and substrates. The damage criteria, which are used to determine element removal in the oxide layer, can help to show the remaining unbroken oxide layer between the particle and substrate, which ultimately reduces the interfacial strength of the sprayed material. Brittle cracking was modeled using the Rankine criterion [50,51] that assumes that cracks form when the maximum principal tensile stress exceeds the tensile strength of the brittle material.

In this material model, crack detection is based on mode-I fracture energy (tension softening/stiffening), and the crack propagation is based on both mode-I and mode-II fracture energies (shear softening/retention) [51]. The failure stress, mode-I fracture energy, and brittle failure were calculated using molecular dynamics simulations. Surface-to-surface explicit interaction was used with hard contact interactions in the normal direction and friction loss (Coulomb friction coefficient of 0.3) in the tangential direction. The entire friction energy was converted into dissipated heat in the system, which contributes to the overall temperature of the system.

Table 1
6061 aluminum alloy and $\gamma - Al_2O_3$ Properties used in cold spray particle impact simulation.

6061 Al Properties [44]			
Density	2700 kg/m^3	JC Damage Constant, d_1	− 0.57
Young's Modulus	68.3 *GPa*	JC Damage Constant, d_2	1.45
Poisson's Ratio	0.33	JC Damage Constant, d_3	0.47
JC Constant, A	270 *MPa*	JC Damage Constant, d_4	0.011
JC Constant, B	154.3 *MPa*	JC Damage Constant, d_5	1.6
JC Constant, n	0.239	Reference Strain Rate, $\dot{\varepsilon}_0$	1
JC Constant, m	1.42	Specific Heat Capacity, C_p	925 J/kgK
JC Constant, C_1	0.002	Expansion Rate, α	24×10^{-6} $1/K$
JC Constant, C_2	0.029	Thermal Conductivity, λ	205 W/mK
Critical Strain Rate, $\dot{\varepsilon}_c$	597	Inelastic Heat Fraction	0.9
Melting Temp, T_m	925	Transition Temp, T_t	298
$\gamma-$ Alumina Properties			
Density [47]	3650 kg/m^3	Failure Stress	34.46 *GPa*
Young's Modulus	260 *GPa*	Mode I Fracture Energy	3.63 N/m
Poisson's Ratio [47]	0.24	Brittle Failure	3.78 Å
Brittle Shear, e [47]	0.319	Brittle Shear, p [47]	1

4. Results and discussion

4.1. Temperature distributions due to powder impacts

The temperature distributions that were obtained from the finite element simulations of a single 6061 Al powder contact at a critical velocity of 800 m/s are presented in Fig. 5. These show multiple views of the temperature profiles induced by particle contact for durations of 200 ns. Note that, due to differences in the thermal properties, the temperature profiles in the oxide layers are initially different from those in the 6061 Al alloy. However, after an initial transient period, the maximum temperature in the system reaches a plateau at 781 K, which is still well below the melting temperature of the 6061 Al alloy (853–923 K) [52]. The nanosecond time scales involved in the heating to steady state conditions in Fig. 5 are much slower than the picosecond timescales required for dynamic crack growth to occur across the 5-nm aluminum oxide thin films (on the powder surface) during contact due to cold spray. This shows that, for the timescales in the cold spray process, melting does not play a significant role. However, this temperature is above the recrystallization temperature of 6061 Al which enables diffusion and diffusion bonding to occur in the regions of particle and substrate impact.

4.2. Molecular dynamics simulations of oxide layer

To efficiently capture the nanoscale behavior of the oxide-layer, we employed MD to obtain the fundamental material properties needed for the finite element simulation. Size-specific mechanical strength, young's modulus, and strain to failure of the oxide-layer, were used in the finite element models, to establish a platform to study the role of oxide layer in the robustness of a variety of metallic powders during the cold spray

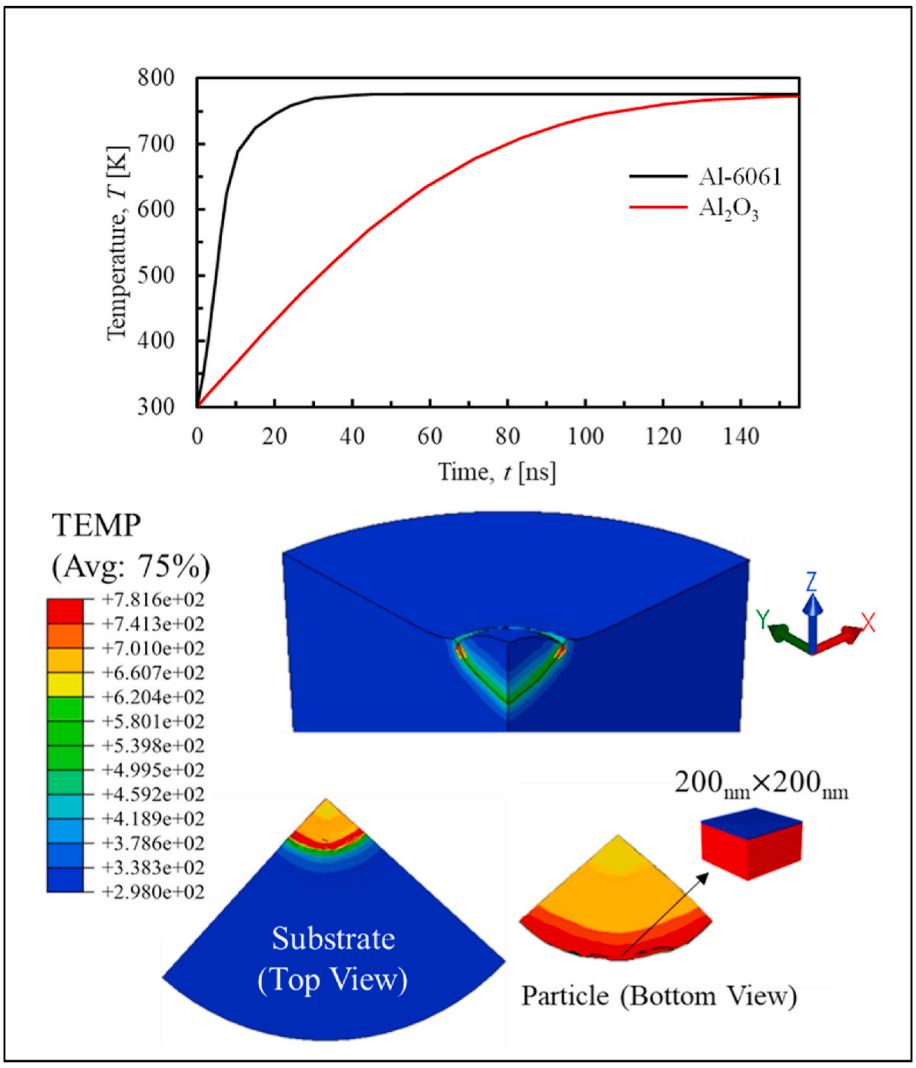

Fig. 5. Temperature increase in the substrate (solid black) and oxide layer (solid red) during cold spray impact of nanoscale oxide layer on a thick aluminum substrate, computed from heat transfer simulations. The timescale of the heat transfer is in nanoseconds range, which is much higher than picoseconds timescale of crack propagation. (For interpretation of the references to color in this figure legend, the reader is referred to the Web version of this article.)

process. As shown in Fig. 4(c), there are regions of spinel crystal structures that are either Al_2O_3 in the form of γ-alumina, or spinel (Mg, Al)$_2O_3$. We simplify the model to an all γ-alumina structure with the thickness of 5 nm and determined the ultimate strength to be 34.46 GPa in the strain-rates applicable in aluminum powder-substrate CS incidents. The Young's modulus of 260 closely matching experimentally obtained measurements [53]. Fig. 6 shows stress strain curve of this model.

4.3. Stress states and deformation/cracking phenomena

The results of the finite element simulations of oxide covered powder impacts at 800 m/s are presented in Figs. 7 and 8. The simulations show evidence of cracking through the oxide layers in the particle and the substrate, and unfractured oxide segments are apparent in Fig. 7. Also, the alumina layer is least likely to fracture at the center or "south pole" (near the impact location in the oxide layer) of the particle impact. This is consistent with measurements of oxide leftover in physical cold spray particle impacts of a perpendicular impact on a flat substrate [16].

It should be noted that the plots of the maximum principal stresses in regions around the south pole do not exceed the stresses required for the failure of the oxide. However, the differences between the maximum principal stresses and the critical conditions are relatively small. Hence,

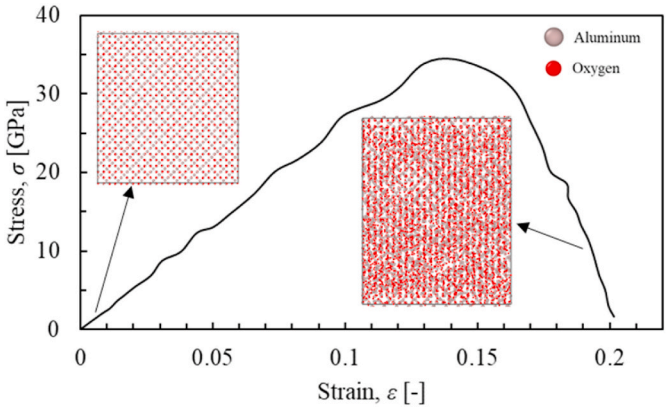

Fig. 6. Stress-strain curve of a 5 nm thick γ-alumina obtained from application of tensile stresses along the C-axis, i) Initial configuration of the 5 nm γ-alumina, ii) Failed and elongated γ-alumina nanocrystal by application of tensile stress.

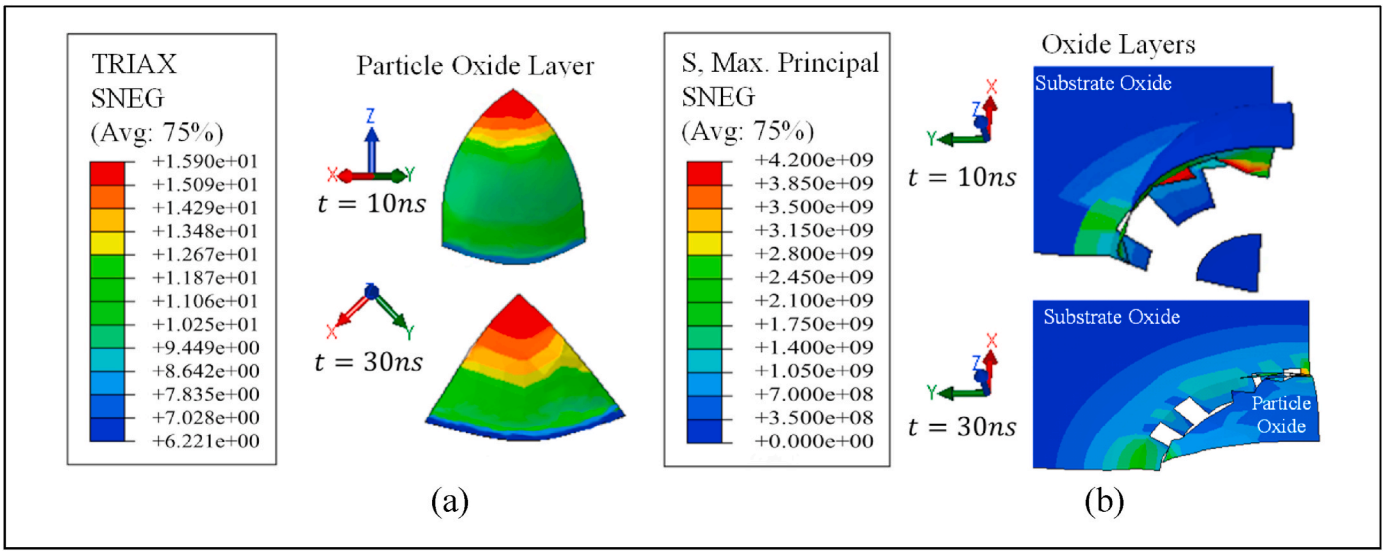

Fig. 7. (a) Triaxiality in the powder oxide layer, (b) maximum principal stress for the substrate and powder oxide layers. The triaxiality shows that regions near the impact zone have lower triaxiality which means that those areas have higher temperature and more plastic like behavior, but since it is still lower than 6, it is within the brittle fracture range. Maximum principal stresses show low to zero stresses near the top regions of the oxide layer, along with remaining fragments of the oxide in the south pole.

the transition from highly deformed states to cracked states may occur rapidly in the regions with high principal stresses and stress gradients (Fig. 7).

Since brittle fracture is more likely to occur in regions with high stress triaxiality [50,51], it is of interest to examine the triaxiality associated with the alumina-covered 6061 Al powder impacts at the critical velocity of 800 m/s. Plots of the triaxiality ratio, which is the ratio of the mean stress/hydrostatic pressure to the von Mises stress, are presented in Figure 7a. These reveal the areas in which brittle fracture is most likely to occur. The stress triaxiality values obtained for the 6061 Al alloy (in both the particle and substrate regions) were generally between 1 and 3, while those of the oxide layers were typically between 6.5 and 19. Hence, brittle cracking is most likely to occur in the alumina layers subjected to fracture critical impacts by the incident oxide-covered 6061 Al particles. However, the regions closer to the top-center (North poles) experience higher triaxiality than those that are farther away.

As shown in Figure 7b, after about 10 ns after the impact, high stresses in the oxide layers are sufficient to cause fracture at the interface of the particle and substrate oxides. However, outside the region of impact (in the substrate oxide), the high stresses that are induced in the substrate oxide films can be enough to initiate fracture in the substrate. Hence, oxide cracking may initiate in either the substrate oxide layers, or the powder oxide layer, or both, depending on the local stress distributions that are induced by the incident powder contacts due to cold spray.

It is important to examine the stress states around the regions of oxide-covered powder contact (Fig. 8). Our finite element results show that, within the inner areas, the ratios of the normal stresses to the shear stresses were greater than those within the outer regions (Fig. 8). Hence, in the regions near the south poles, the normal stresses dominated, while in the outer regions, the shear stresses dominated the stress fields. The shear stresses also have the effect of extruding the materials out of the edges of the splats, during the splat evolution that accompanies powder contact and deformation. This extrusion process is also associated with the progressive shear extrusion and fracture of alumina segments from the sides of the splats.

Hence, as shown in the schematic of the cold spray powder impact in Fig. 8, the stages of deformation and cracking that are associated with powder particle contacts are the following. First, the particles come into elastic contact; this is followed by plastic deformation and cracking phenomena in regions around the resulting splat; shear-controlled extrusion and cracking, while the exposure of bare metal surfaces (following the cracking of the alumina) can result in bonding and mechanical interlocking of cold sprayed structures.

4.4. Parametric study

The effect of several parameters on the amount of oxide that would remain trapped between the particle and the substrate is presented here. These parameters are powder velocity, powder size, and oxide thickness. The reason for selecting these parameters is that the powder size is not uniform and depending on the processing method, air exposure, and other parameters, the thickness of the oxide varies. And finally, the effects of different impact velocities (in the range between critical to erosion velocity) on the stress states and deformation processes and their corresponding impacts on the oxide trapping phenomenon were investigated. The results are presented in Fig. 9. The radii of the remaining unbroken oxide layers (near the South pole) decreased with increasing impact velocity, while the strains in the unbroken oxide layer increased with increasing impact velocity, as shown in Figure 9a. This is consistent with experimental results that showed increased bond strengths at higher velocities [30,51]. Also, the higher stresses induced at higher velocities should increase the layer deformation, and thus reduce the trapped oxide thickness.

Plots of the dependence of the ratio of the unbroken oxide radius to particle radius and the total strain dependence on the particle radius are shown in Figure 9b. It is revealed that the ratio of the trapped oxide layer diameter to particle diameter was not significantly affected by the powder size which is reasonable since larger particles have more surface area that undergoes pure compression with close to no shear stress applying on them.

However, the thickness of the unfractured oxide layer and the strains in the unfractured oxide layer decreased with increasing oxide thickness, as shown in Figure 9c. This can be understood by considering the tensile stresses that the oxide layer is subjected to. Since thinner oxide layers are subjected to lower bending stresses, more segments of the thinner layers should remain unfractured when subjected to similar loads. The converse is true for thicker films. Hence, more segments of the thicker alumina layers will remain unfractured when subjected to the

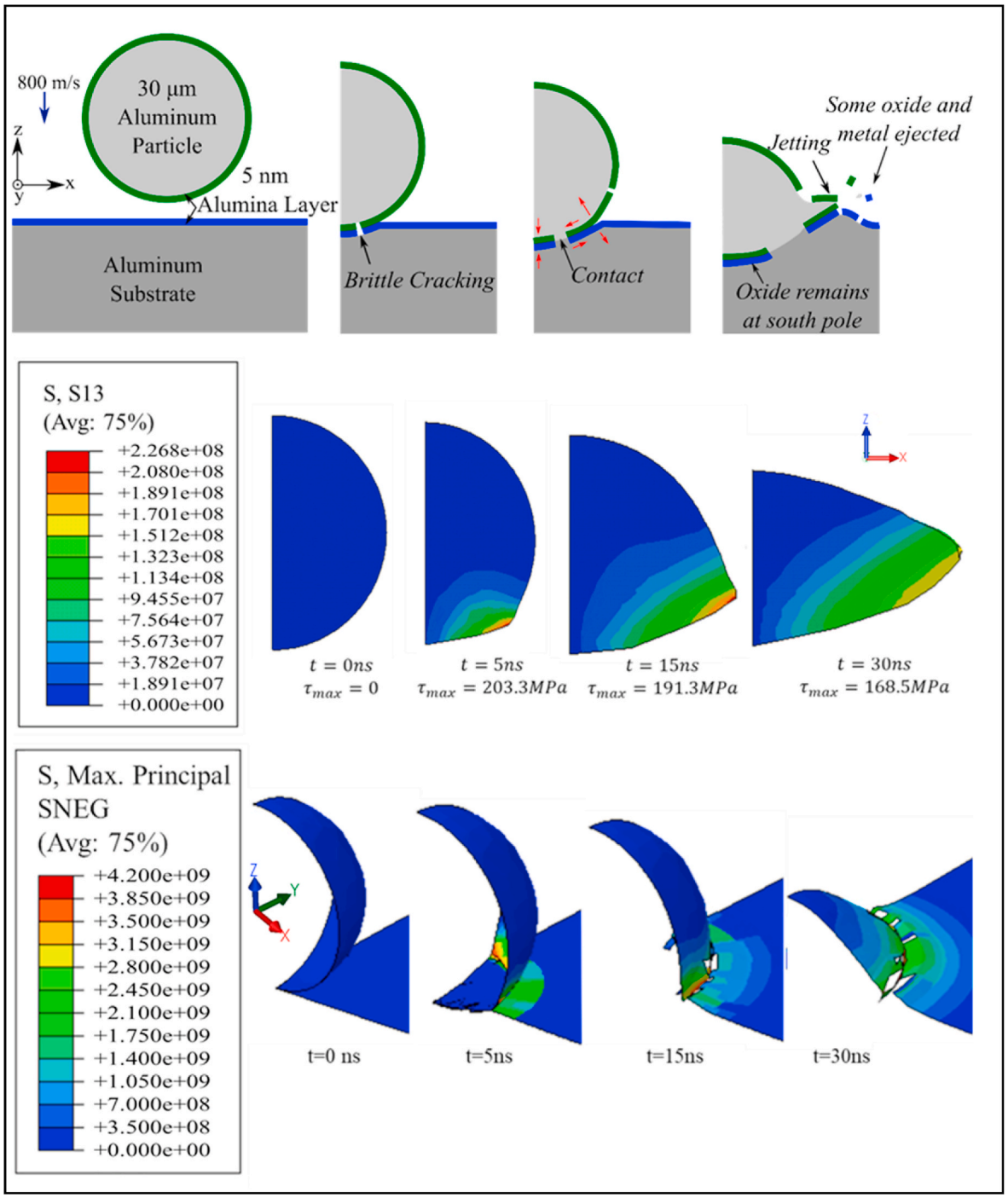

Fig. 8. (Top) schematic of the cold spray (middle) shear stress distribution in the particle, (bottom) maximum principal stress in the oxide layer during the deformation due to impact. Shear stresses show that jetting occurs at the outer regions of the impact zone more than regions closer to the south pole of the powder. Additionally, principal stresses are highest at the intersection of the powder/substrate impact zone, although there are still considerable amounts of stresses around edge of the intersection.

same incident particle velocities.

5. Conclusions

1. MD simulations have been used to extract the young's modulus, the tensile strength, strain to failure and the toughness of the gamma aluminum oxide films (with a thickness of ~5-nm). These have been shown, respectively, to be 288 GPa, 35.6 GPa, 0.20, and 3.84 N/m for the nanoscale topical gamma alumina layer.
2. The residual oxide film thickness and strains decrease with increasing particle velocity. The strains in the unfractured oxide layers increase with increasing thickness of the unfractured oxide layers. Furthermore, since higher strain rates increase the ultimate strengths and toughness values of the alumina films, higher strain rates (corresponding to faster particle velocities) result in thicker trapped residual films within the cold spray contacts.
3. While compressive strains at the South pole limit oxide cracking, tensile and mixed loading below the equator can promote the cracking of the oxide layers on the substrate and the particles. The

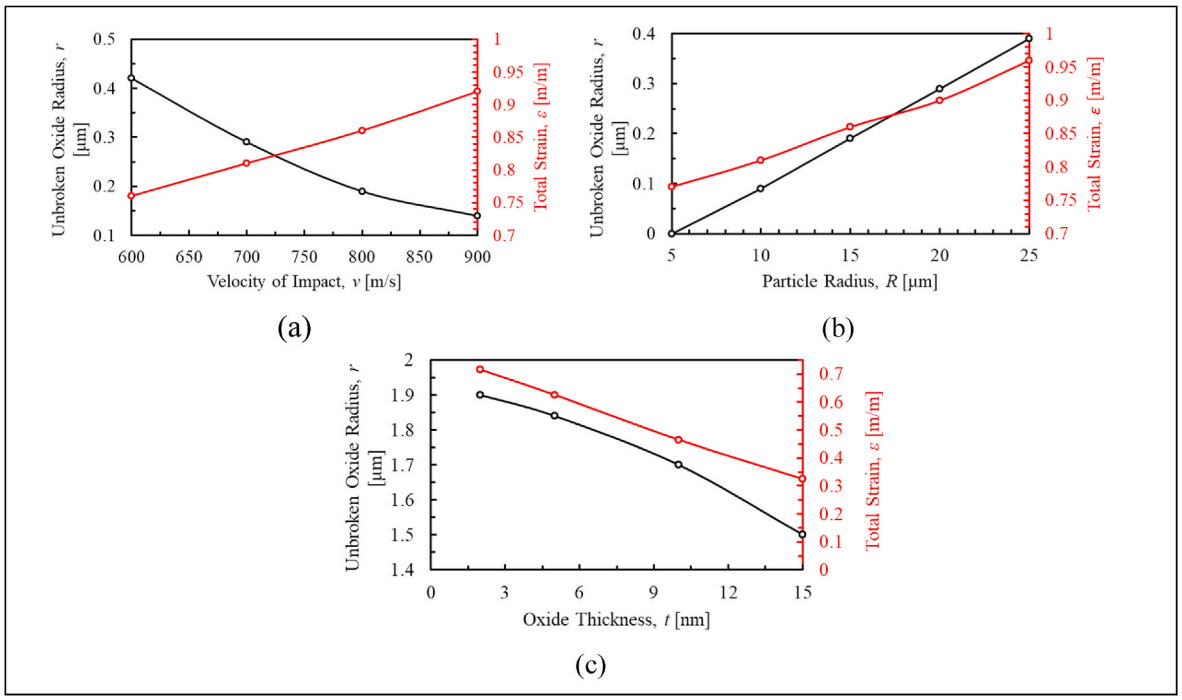

Fig. 9. Variation of unfractured pieces as functions of impact velocity, and particle radius for oxide layer (a, b); Variation of unfractured oxide segments as functions of oxide thickness (c).

shear stresses at the edges of the splats can also lead to the extrusion of the splats and the cracking of oxide layers (on the surfaces of cold sprayed 6061 Al powders) that gives rise to contact between the freshly exposed substrate surfaces.

4. The FEA and the MD simulations also reveal that the incident particle velocity and the gamma aluminum oxide thickness are negatively correlated with the area of unfractured aluminum oxide. However, the failure strengths of the oxide film are positively correlated. Hence, the current results confirm the important role of the nano-scale gamma aluminum oxide layers on the failure strength of cold sprayed 6061 Al powders on similar substrates.

CRediT authorship contribution statement

A. Navabi: Conceptualization, Methodology, Data Curation, Writing – original draft. **M. Vandadi:** Conceptualization, Investigation, Methodology, Data Curation, Writing – original draft. **T. Bond:** Methodology, Data Curation, Writing – original draft. **V. Rahneshin:** Data Curation, Writing – original draft. **J. Obayemi:** Methodology, Writing – review & editing. **R. Ahmed:** Methodology. **J. E. Oghenevweta:** Conceptualization, Methodology, Writing – original draft. **V. Champagne:** Writing – review. **N. Rahbar:** Conceptualization, Writing – review & editing, Project administration, Validation, Supervision, Funding acquisition. **W. O. Soboyejo:** Conceptualization, Writing – review & editing, Project administration, Validation, Supervision, Funding acquisition.

Declaration of competing interest

The authors declare that they have no known competing financial interests or personal relationships that could have appeared to influence the work reported in this paper.

Acknowledgements

This research was supported by the Army Research Lab (ARL) Grant No. W911NF-19-2-0108. The authors are also grateful to the Army Research Lab Cold Spray Program Manager, Matt Siopis, for his encouragement and support. The FIB results were obtained with the support of the Harvard Center for Nanoscale Systems (CNS). Finally, the XPS results were obtained in the lab of Professor Ronald Grimm at WPI.

References

[1] V.K. Champagne, The Cold Spray Materials Deposition Process: Fundamentals and Applications, Elsevier, 2007.
[2] A. Papyrin, V. Kosarev, S. Klinkov, A. Alkhimov, V.M. Fomin, Cold Spray Technology, Elsevier, 2006.
[3] T.H. Van Steenkiste, J.R. Smith, R.E. Teets, J.J. Moleski, D.W. Gorkiewicz, R. P. Tison, D.R. Marantz, K.A. Kowalsky, W.L. Riggs, P.H. Zajchowski, B. Pilsner, R. C. McCune, K.J. Barnett, Kinetic Spray Coatings, Surface, and Coatings Technology, 111, 1999, pp. 62–71, https://doi.org/10.1016/S0257-8972(98)00709-9.
[4] R.C. Dykhuizen, M.F. Smith, D.L. Gilmore, R.A. Neiser, X. Jiang, S. Sampath, Impact of high velocity cold spray particles, J. Therm. Spray Technol. 8 (1999) 559–564, https://doi.org/10.1361/105996399770350250.
[5] A.P. Alkhimov, V.F. Kosarev, A.N. Papyrin, Gas-dynamic spraying. An experimental study of the spraying process, J. Appl. Mech. Tech. Phys. 39 (1998) 318–323, https://doi.org/10.1007/BF02468100.
[6] T. Schmidt, F. Gärtner, H. Assadi, H. Kreye, Development of a generalized parameter window for cold spray deposition, Acta Mater. 54 (2006) 729–742, https://doi.org/10.1016/j.actamat.2005.10.005.
[7] A. Moridi, S.M. Hassani-Gangaraj, M. Guagliano, M. Dao, Cold spray coating: review of material systems and future perspectives, Surf. Eng. 30 (2014) 369–395, https://doi.org/10.1179/1743294414Y.0000000270.
[8] H. Assadi, F. Gärtner, T. Stoltenhoff, H. Kreye, Bonding mechanism in cold gas spraying, Acta Mater. 51 (2003) 4379–4394, https://doi.org/10.1016/S1359-6454(03)00274-X.
[9] M. Grujicic, C.L. Zhao, W.S. DeRosset, D. Helfritch, Adiabatic shear instability-based mechanism for particles/substrate bonding in the cold-gas dynamic-spray process, Mater. Des. 25 (2004) 681–688, https://doi.org/10.1016/j.matdes.2004.03.008.
[10] M. Hassani-Gangaraj, D. Veysset, V.K. Champagne, K.A. Nelson, C.A. Schuh, Adiabatic shear instability is not necessary for adhesion in cold spray, Acta Mater. 158 (2018) 430–439, https://doi.org/10.1016/j.actamat.2018.07.065.
[11] T. Hussain, D.G. McCartney, P.H. Shipway, D. Zhang, Bonding mechanisms in cold spraying: the contributions of metallurgical and mechanical components, J. Therm. Spray Technol. 18 (2009) 364–379, https://doi.org/10.1007/s11666-009-9298-1.
[12] V.K. Champagne, D. Helfritch, P. Leyman, S. Grendahl, B. Klotz, Interface material mixing formed by the deposition of copper on aluminum by means of the cold spray process, J. Therm. Spray Technol. 14 (2005) 330–334, https://doi.org/10.1361/105996305X59332.

[13] F. Meng, D. Hu, Y. Gao, S. Yue, J. Song, Cold-spray bonding mechanisms and deposition efficiency prediction for particle/substrate with distinct deformability, Mater. Des. 109 (2016) 503–510, https://doi.org/10.1016/j.matdes.2016.07.103.

[14] J. Lienhard, C. Crook, M.Z. Azar, M. Hassani, D.R. Mumm, D. Veysset, D. Apelian, K.A. Nelson, V. Champagne, A. Nardi, C.A. Schuh, L. Valdevit, Surface oxide and hydroxide effects on aluminum microparticle impact bonding, Acta Mater. 197 (2020) 28–39, https://doi.org/10.1016/j.actamat.2020.07.011.

[15] M. Hassani-Gangaraj, D. Veysset, K.A. Nelson, C.A. Schuh, Impact-bonding with aluminum, silver, and gold microparticles: toward understanding the role of native oxide layer, Appl. Surf. Sci. 476 (2019) 528–532, https://doi.org/10.1016/j.apsusc.2019.01.111.

[16] Y. Ichikawa, R. Tokoro, M. Tanno, K. Ogawa, Elucidation of cold-spray deposition mechanism by auger electron spectroscopic evaluation of bonding interface oxide film, Acta Mater. 164 (2019) 39–49, https://doi.org/10.1016/j.actamat.2018.09.041.

[17] Y. Ichikawa, K. Ogawa, Effect of substrate surface oxide film thickness on deposition behavior and deposition efficiency in the cold spray process, J. Therm. Spray Technol. 24 (2015) 1269–1276, https://doi.org/10.1007/s11666-015-0299-y.

[18] Y. Xie, S. Yin, C. Chen, M.-P. Planche, H. Liao, R. Lupoi, New insights into the coating/substrate interfacial bonding mechanism in cold spray, Scripta Mater. 125 (2016) 1–4, https://doi.org/10.1016/j.scriptamat.2016.07.024.

[19] C.-J. Li, H.-T. Wang, Q. Zhang, G.-J. Yang, W.-Y. Li, H.L. Liao, Influence of spray materials and their surface oxidation on the critical velocity in cold spraying, J. Therm. Spray Technol. 19 (2010) 95–101, https://doi.org/10.1007/s11666-009-9427-x.

[20] S. Rahmati, R.G. Veiga, A. Zúñiga, B. Jodoin, A numerical approach to study the oxide layer effect on adhesion in cold spray, J. Therm. Spray Technol. (2021) 1–15, https://doi.org/10.1007/s11666-021-01245-4.

[21] A.A. Hemeda, C. Zhang, X.Y. Hu, D. Fukuda, D. Cote, I.M. Nault, A. Nardi, V. K. Champagne, Y. Ma, J.W. Palko, Particle-based simulation of cold spray: influence of oxide layer on impact process, Additive Manufacturing 37 (2021) 101517, https://doi.org/10.1016/j.addma.2020.101517.

[22] L. Nguyen, T. Hashimoto, D.N. Zakharov, E.A. Stach, A.P. Rooney, B. Berkels, G. E. Thompson, S.J. Haigh, T.L. Burnett, Atomic-scale insights into the oxidation of aluminum, ACS Appl. Mater. Interfaces 10 (2018) 2230–2235, https://doi.org/10.1021/acsami.7b17224.

[23] B.A. Bedard, T.J. Flanagan, A.T. Ernst, A. Nardi, A.M. Dongare, H.D. Brody, V. K. Champagne, S.-W. Lee, M. Aindow, Microstructure and micromechanical response in gas-atomized Al 6061 alloy powder and cold-sprayed splats, J. Therm. Spray Technol. 27 (2018) 1563–1578, https://doi.org/10.1007/s11666-018-0785-0.

[24] A.G. Gavras, D.A. Lados, V.K. Champagne, R.J. Warren, Effects of processing on microstructure evolution and fatigue crack growth mechanisms in cold-spray 6061 aluminum alloy, Int. J. Fatig. 110 (2018) 49–62, https://doi.org/10.1016/j.ijfatigue.2018.01.006.

[25] M.R. Rokni, C.A. Widener, V.R. Champagne, Microstructural evolution of 6061 aluminum gas-atomized powder and high-pressure cold-sprayed deposition, J. Therm. Spray Technol. 23 (2014) 514–524, https://doi.org/10.1007/s11666-013-0049-y.

[26] L.P.H. Jeurgens, W.G. Sloof, F.D. Tichelaar, E.J. Mittemeijer, Composition and chemical state of the ions of aluminum-oxide films formed by thermal oxidation of aluminum, Surf. Sci. 506 (3) (2002) 313–332, https://doi.org/10.1016/S0039-6028(02)01432-2.

[27] A. Jimenez-Gonzalez, D. Schmeisser, Preparation, and spectroscopic characterization of γ-Al2O3 thin films, Surf. Sci. 250 (1–3) (1991) 59–70, https://doi.org/10.1016/0039-6028(91)90709-2.

[28] A. Bianconi, R.Z. Bachrach, S.B.M. Hagstrom, S.A. Flodström, Al-Al 2 O 3 interface study using surface soft-x-ray absorption and photoemission spectroscopy, Phys. Rev. B 19 (6) (1979) 2837, https://doi.org/10.1103/PhysRevB.19.2837.

[29] A.T. Ernst, P. Kerns, A. Nardi, H.D. Brody, A.M. Dongare, S.W. Lee, V. K. Champagne, S.L. Suib, M. Aindow, Surface states of gas-atomized Al 6061 powders–Effects of heat treatment, Appl. Surf. Sci. 534 (2020) 147643, https://doi.org/10.1016/j.apsusc.2020.147643.

[30] H.P. Leighly Jr., A. Alam, The oxidation of dilute alloys of magnesium in aluminium, J. Phys. F Met. Phys. 14 (6) (1984) 1573, https://doi.org/10.1088/0305-4608/14/6/024.

[31] Ping Fu, Wenzhong Lu, Lei Wen, Ke Wu, Yong Xu, Jiamin Wu, Thermal stability and microstructure characterization of MgAl2O4 nanoparticles synthesized by reverse microemulsion method, Mater. Res. 16 (4) (2013) 844–849, https://doi.org/10.1590/S1516-14392013005000062.

[32] T.R. Shan, B.D. Devine, T.W. Kemper, S.B. Sinnott, S.R. Phillpot, Charge-optimized many-body potential for the hafnium/hafnium oxide system, Phys. Rev. B 81 (12) (2010) 125328, https://doi.org/10.1103/PhysRevB.81.125328.

[33] S.W. Rick, S.J. Stuart, B.J. Berne, Dynamical fluctuating charge force fields: application to liquid water, J. Chem. Phys. 101 (7) (1994) 6141–6156, https://doi.org/10.1063/1.468398.

[34] S. Plimpton, Fast parallel algorithms for short-range molecular dynamics, J. Comput. Phys. 117 (1) (1995) 1–19, https://doi.org/10.1006/jcph.1995.1039.

[35] V.K. Champagne, D.J. Helfritch, S.P.G. Dinavahi, P.F. Leyman, Theoretical and experimental particle velocity in cold spray, J. Therm. Spray Technol. 20 (2011) 425–431, https://doi.org/10.1007/s11666-010-9530-z.

[36] H. Koivuluoto, J. Larjo, D. Marini, G. Pulci, F. Marra, Cold-sprayed Al6061 coatings: online spray monitoring and influence of process parameters on coating properties, Coatings 10 (2020) 348, https://doi.org/10.3390/coatings10040348.

[37] D. Nélias, J. Xie, H.W.-L. Berre, Y. Ichikawa, K. Ogawa, Simulation of the cold spray deposition process for aluminum and copper using Lagrangian, ALE and CEL methods, in: Thermomechanical Industrial Processes, John Wiley & Sons, Ltd, 2014, pp. 321–358, https://doi.org/10.1002/9781118578759.ch7.

[38] W.-Y. Li, H. Liao, C.-J. Li, H.-S. Bang, C. Coddet, Numerical simulation of deformation behavior of Al particles impacting on Al substrate and effect of surface oxide films on interfacial bonding in cold spraying, Appl. Surf. Sci. 253 (2007) 5084–5091, https://doi.org/10.1016/j.apsusc.2006.11.020.

[39] E. Lin, Q. Chen, O.C. Ozdemir, V.K. Champagne, S. Müftü, Effects of interface bonding on the residual stresses in cold-sprayed Al-6061: a numerical investigation, J. Therm. Spray Technol. 28 (2019) 472–483, https://doi.org/10.1007/s11666-019-00827-7.

[40] X. Wang, F. Feng, M.A. Klecka, M.D. Mordasky, J.K. Garofano, T. El-Wardany, A. Nardi, V.K. Champagne, Characterization, and modeling of the bonding process in cold spray additive manufacturing, Additive Manufacturing 8 (2015) 149–162, https://doi.org/10.1016/j.addma.2015.03.006.

[41] J. Xie, D. Nélias, H. Walter-Le Berre, K. Ogawa, Y. Ichikawa, Simulation of the cold spray particle deposition process, J. Tribol. 137 (2015), https://doi.org/10.1115/1.4030257.

[42] B. Yildirim, H. Fukanuma, T. Ando, A. Gouldstone, S. Müftü, A numerical investigation into cold spray bonding processes, J. Tribol. 137 (2015), https://doi.org/10.1115/1.4028471.

[43] B. Yıldırım, A. Hulton, S.A. Alavian, T. Ando, A. Gouldstone, S. Müftü, On simulation of multi-particle impact interactions in the cold spray process, in: American Society of Mechanical Engineers Digital Collection, 2013, pp. 83–85, https://doi.org/10.1115/IJTC2012-61202.

[44] A. Alizadeh Dehkharghani, Tuning Johnson-Cook material model parameters for impact of high velocity, micron scale aluminum particles. https://repository.library.northeastern.edu/files/neu:cj82pb67g, 2016. (Accessed 8 August 2020).

[45] V. Lemiale, P.C. King, M. Rudman, M. Prakash, P.W. Cleary, M.Z. Jahedi, S. Gulizia, Temperature and strain rate effects in cold spray investigated by smoothed particle hydrodynamics, Surf. Coating. Technol. 254 (2014) 121–130, https://doi.org/10.1016/j.surfcoat.2014.05.071.

[46] Q. Chen, A. Alizadeh, W. Xie, X. Wang, V. Champagne, A. Gouldstone, J.-H. Lee, S. Müftü, High-strain-rate material behavior and adiabatic material instability in impact of micron-scale Al-6061 particles, J. Therm. Spray Technol. 27 (2018) 641–653, https://doi.org/10.1007/s11666-018-0712-4.

[47] A. Tasdemirci, I.W. Hall, Numerical and experimental studies of damage generation in multi-layer composite materials at high strain rates, Int. J. Impact Eng. 34 (2007) 189–204, https://doi.org/10.1016/j.ijimpeng.2005.08.010.

[48] M. Hassani-Gangaraj, D. Veysset, K.A. Nelson, C.A. Schuh, In-situ observations of single micro-particle impact bonding, Scripta Mater. 145 (2018) 9–13, https://doi.org/10.1016/j.scriptamat.2017.09.042.

[49] L.E. Kinsler, A.R. Frey, A.B. Coppens, J.V. Sanders, Fundamentals of Acoustics, fourth ed., Wiley, Wiley.Com, 1999. https://www.wiley.com/en-us/Fundamentals+of+Acoustics%2C+4th+Edition-p-9780471847892.

[50] W.J.M. Rankine, II. On the stability of loose earth, Phil. Trans. Roy. Soc. Lond. 147 (1857) 9–27, https://doi.org/10.1098/rstl.1857.0003.

[51] A cracking model for concrete and other brittle materials, n.d. https://abaqus-docs.mit.edu/2017/English/SIMACAETHERefMap/simathe-c-cracking.htm.

[52] ASM handbook volume 2: properties and selection: nonferrous alloys and special-purpose materials - ASM international, (n.d.), https://www.asminternational.org/materials-resources/results/-/journal_content/56/10192/06182G/PUBLICATION.

[53] M.K. Tripp, C. Stampfer, D.C. Miller, T. Helbling, C.F. Herrmann, C. Hierold, K. Gall, S.M. George, V.M. Bright, The mechanical properties of atomic layer deposited alumina for use in micro- and nano-electromechanical systems, Sens. Actuators, A 130–131 (2006) 419–429, https://doi.org/10.1016/j.sna.2006.01.029.